ACS NANO
Cite This: ACS Nano 2020, 14, 328–336
www.acsnano.org

ARTICLE

Electrotunable Nanoplasmonics for Amplified Surface Enhanced Raman Spectroscopy

Ye Ma,[†,‡] Debabrata Sikdar,[†,§] Aleksandra Fedosyuk,[†] Leonora Velleman,[†] Daniel J. Klemme,[∥] Sang-Hyun Oh,[∥] Anthony R. J. Kucernak,[†] Alexei A. Kornyshev,[*,†,⊥] and Joshua B. Edel[*,†]

[†]Department of Chemistry, Imperial College London, Molecular Sciences Research Hub, White City Campus, London W12 0BZ, U.K.

[‡]School of Materials Science and Engineering, Ocean University of China, Qingdao, 266100, China

[§]Department of Electronics and Electrical Engineering, Indian Institute of Technology Guwahati, Guwahati 781039, India

[∥]Department of Electrical and Computer Engineering, University of Minnesota, Minneapolis, Minnesota 55455, United States

[⊥]Thomas Young Centre for Theory and Simulation of Materials, Imperial College London, South Kensington Campus, London SW7 2AZ, U.K.

Supporting Information

ABSTRACT: **Tuning the properties of optical metamaterials in real time is one of the grand challenges of photonics. Being able to do so will enable a class of adaptive photonic materials for use in applications such as surface enhanced Raman spectroscopy and reflectors/absorbers. One strategy to achieving this goal is based on the electrovariable self-assembly and disassembly of two-dimensional nanoparticle arrays at a metal | liquid interface. As expected, the structure results in plasmonic coupling between NPs in the array but perhaps as importantly between the array and the metal surface. In such a system, the density of the nanoparticle array can be reversibly controlled by the variation of electrode potential. Theory suggests that due to a collective plasmon-coupling effect less than 1 V variation of electrode potential can give rise to a dramatic simultaneous change in optical reflectivity from ∼93% to ∼1% and the amplification of the SERS signal by up to 5 orders of magnitude. This is experimentally demonstrated using a platform based on the voltage-controlled assembly of 40 nm Au-nanoparticle arrays at a TiN/Ag electrode in contact with an aqueous electrolyte. We show that all the physics underpinning the behavior of this platform works precisely as suggested by the proposed theory, setting the electrochemical nanoplasmonics as a promising direction in photonics research.**

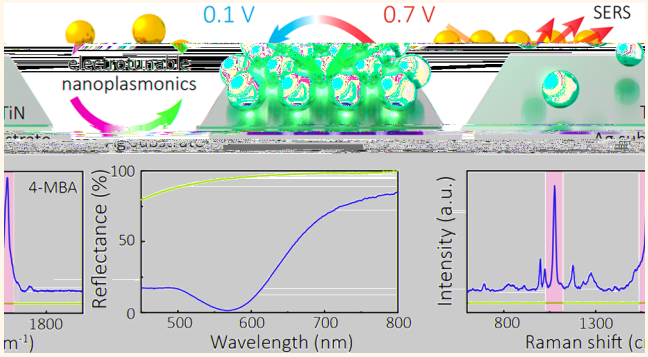

KEYWORDS: *electrotunable, metasurface, plasmonics, surface enhanced Raman spectroscopy, nanoparticles, self-assembly*

The plasmonic coupling of metallic nanostructures under the excitation of incident light has not only drawn substantial interest[1−3] but also looks promising for applications in optical sensing,[4−6] solar energy,[7] biomedical therapy,[8,9] and especially surface-enhanced Raman spectroscopy (SERS).[10−16] The vibrational Raman fingerprints of target molecules can be enhanced several orders of magnitude because of the synergistic coupling of localized surface plasmon resonances (LSPR) of nanoparticles (NPs),[17,18] surface modified planar substrates,[19] or a combination of both.[3,20,21] Previous reports based on deposited NPs[22] or lithographic features[10,23] on dry substrates have beautifully demonstrated that the surrounding media,[24] metal species,[11] size,[25] shape,[26] interparticle distance,[24,27] and the gap between the substrate and NPs[3] are crucial for the resonance strength, frequency, and the resultant SERS signals. The latter is caused by the local near-field enhancement ("hot spots") inside or around these nanostructures.

Some of those structures may be fixed/nanofabricated,[28] others—self-assembled.[29] One of the challenges is to adjust the structures in situ enabling the tuning of the intensity of the hot spots for maximizing SERS signals.[30] Among many methods such as mechanically[31] or thermally[32−34] induced deformation of the nanostructures, or in the case of wet systems—changing pH[35] or chemical concentrations[36] of the solution can reconfigure the NP assemblies. Particularly interesting is voltage-controlled tuning of the structure of adsorbed NP

Received: July 4, 2019
Accepted: December 6, 2019
Published: December 6, 2019

DOI: 10.1021/acsnano.9b05257
ACS Nano 2020, 14, 328−336

Figure 1. Working principles of electrovariable surface enhanced Raman spectroscopy. (a) Scheme of the experimental setup for the switchable assembly of 40 nm NPs, functionalized by negatively charged 4-MBA ligands, on TiN/Ag substrate under low (left) and high (right) applied voltage. When the applied positive potential of the substrate is low, few NPs are assembled, inducing a weak Raman signal (left). A higher positive potential results in a higher NP density which generates Raman hot spots and delivers a stronger SERS signal (right). (b,c) The experimental reflectance spectra (b) and SERS spectra (c) of NPs on TiN/glass at 0.1 and 0.7 V vs PZC (i), NPs on TiN/Ag at 0.1 V vs PZC (ii) and NPs on TiN/Ag at 0.7 V vs PZC (iii). The inset of panel c—ii shows the original intensity of the Raman signal multiplied by 50 for better visibility. Comparison of these curves highlights the effect of complex plasmonic coupling between the nanoparticles and the metallic substrate.

arrays at electrochemical interfaces.[37,38] This causes minimal disturbance to the system, when tuning the plasmonic coupling. By applying different static[39] or dynamic[40] potentials on the substrate electrodes, researchers can either control the adsorption of ions[40,41] or, for potentials outside of the electrochemical windows of such systems, the electron exchange[39] between NP and the electrodes. Both can affect SERS signals. Our group has previously demonstrated voltage controlled self-assembly of arrays of moderate-size (16 nm) NPs at both liquid | liquid (LLI)[42] and solid | liquid (SLI)[43] interfaces.

In this work, we successfully self-assembled 40 nm NP two-dimensional arrays onto a TiN-coated Ag electrode-substrate within an optical-electrochemical cell. We show that by controlling the electrode potential, both the optical reflectance and SERS spectra can be tuned in real-time. Importantly, the SERS signal can be amplified because of the coupling of NPs in an array and further amplified because of the coupling between NP array and Ag substrate. This is very much different from the literature based around the coupling of static individual NP's to a metallic substrate as the collective coupling of the NPs in the array in our case results in a red-shift in the coupled plasmon resonance and better matches the Raman excitation wavelength, which in turn results in greater SERS intensities. Furthermore, by using our effective media theory (EMT),[44] the optical reflectance spectra can be reproduced, allowing us to reveal information about the structure and interparticle spacing of the NP array in situ. This could in turn be directly correlated to changes in the SERS intensity. Thus, the results that we present below demonstrate fine-tuning of interparticle gaps and the significant amplification of SERS signal. Compared with previously demonstrated SERS active substrates based on NP aggregation, our electrovariable SERS system not only allows for real-time tailorable nanostructures that can be repeatedly used but also facilitates the extra coupling between the metallic substrate and the NP array, further amplifying the SERS signal.

RESULTS AND DISCUSSION

To achieve electrotunability, a planar 125 nm thick Ag substrate with a 5 nm TiN coating acts as the working electrode. A ring-shaped Pt counter electrode and an Ag/AgCl wire reference electrode completes the three-electrode electrochemical cell (Figure S1). The electrodes were embedded in a

DOI: 10.1021/acsnano.9b05257
ACS Nano 2020, 14, 328−336

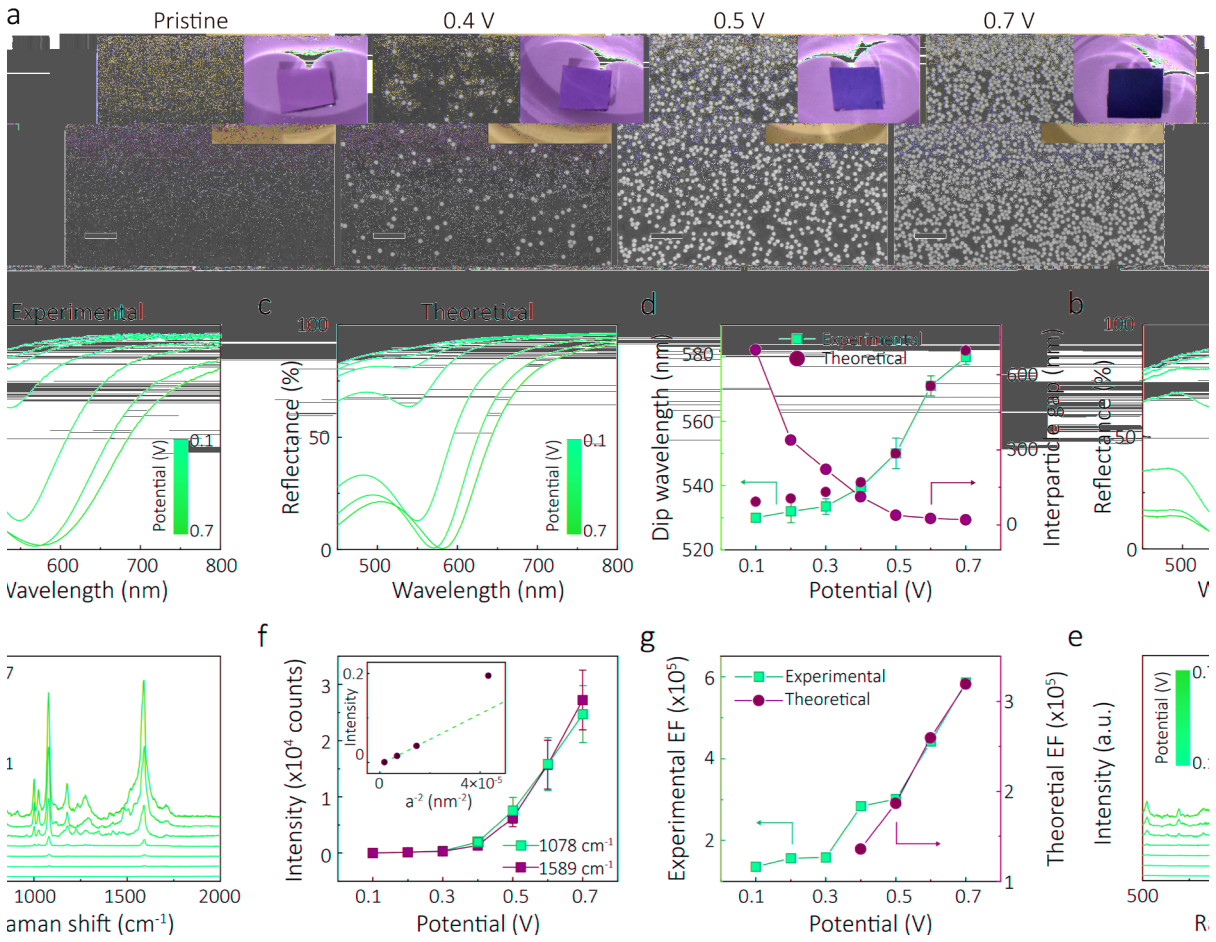

Figure 2. Assembly of nanoparticles by changing the interfacial potentials. (a) SEM of dried samples after NP assembly under indicated potentials; scale bar 200 nm. Digital camera photos (insets) of wet samples after NP assembly on TiN/Ag under indicated potentials. (b) Experimental reflectance spectra of assembling NPs on TiN/Ag under 0.1−0.7 V vs PZC. (c) Theoretically fitted reflectance spectra of assembling NPs on TiN/Ag under 0.1−0.7 V vs PZC. (d) Experimental and theoretically fitted dip wavelength (orange squares) and the theoretically calculated interparticle gap (blue dots) under 0.1−0.7 V vs PZC. (e) Experimental Raman spectra of MBA from the NP array on TiN/Ag under 0.1−0.7 V vs PZC. (f) The intensity of characteristic Raman peaks of 4-MBA at 1078 cm^{-1} (orange) and 1589 cm^{-1} (blue) under 0.1−0.7 V vs PZC. Inset shows the 1078 cm^{-1} Raman peak intensity (I) vs the inverse of the square of the interparticle distance (a^{-2}), extracted from fitting the reflectance data to the theory (cf. panel d), in the interval of 0.1 V between 0.1−0.4 V vs PZC (g) Experimental (orange squares) and theoretically calculated (blue dots) SERS enhancement factor (EF) under 0.1−0.7 V vs PZC. The theoretical EF is not calculated below 0.3 V vs PZC as the gaps are too large to return converging results.

solution containing an electrolyte composed of 4-mercaptobenzoic acid (4-MBA) functionalized 40 ± 3 nm NPs (Figure S2), 20 mM phosphate buffer (PB, pH 6.2), and 20 mM LiCl. A custom-built inverted Raman microscope[45,46] was used to focus a 632.8 nm He−Ne laser to a diffraction limited spot onto the solid−liquid interface and to collect the Raman spectra. A fibreoptic reflectivity probe[47] was also integrated into the cell to simultaneously acquire reflectance spectra at the SLI. These spectra not only quantitatively demonstrate the dramatic color changes during the electro-variable process as we show later but also provide vital structural information about the nanoscale rearrangement of NPs when compared and "decoded" using our EMT.[44]

The potential of zero charge (PZC) of the TiN/Ag substrate is an essential reference point which governs which potentials are needed to bring NPs to and from the SLI.[42,43] PZCs of semiconductor-covered metals can be determined from their flatband potential, E_{fb}. At the flatband potential, there is no band bending due to surface charges, so that this potential is also the potential of zero charge, namely, $E_{fb} = E_{pzc}$.[48] By measuring the capacitance of the TiN/Ag as a function of applied electrochemical potential, we determined that the capacitance−potential variation (Figure S4) followed a Mott−Schottky law: $C_{SC}^{-2} \propto E - E_{PZC} - k_B T/e$, where C_{SC} is the capacitance of the space charge in TiN, E is the applied potential, E_{PZC} is the potential of zero charge, k_B is the Boltzmann constant, and T the absolute temperature. The observed linear relationship indicates that the space charge capacitance of the TiN layer dominates the overall capacitance. The PZC was calculated to be −0.8 V vs Ag/AgCl from the intercepts of a linear fit to the data (Figure S4). Henceforth, all potentials are referenced to the PZC, $\bar{E} = E - E_{PZC}$. In order to ensure that our results were not affected by side-reactions at the electrodes, the minimum and maximum electrochemical potential limits were set so as to ensure that the maximum leakage current across the cell would not exceed 10 μA cm^{-2} over the potential range 0.1−0.7 V vs PZC (Figure S5).

When the potential applied to the substrate is low, NPs do not assemble on the surface. As a result there is no plasmonic coupling between the substrate and NPs, and hence, the

DOI: 10.1021/acsnano.9b05257
ACS Nano 2020, 14, 328−336

corresponding reflectance spectra are identical when compared with pristine TiN/Ag (Figure 1b-ii, black and yellow curves). In addition, no MBA signal could be observed in the Raman spectra (Figure 1c-ii, yellow curve). By switching the substrate to higher potential, 0.7 V vs PZC, the attractive electrostatic forces between the positively charged substrate and the negatively charged NPs construct an energy well in the vicinity of the SLI and results in the self-assembly of NPs into a two-dimensional array on the substrate (Figure 1a, right). This structure results in plasmonic coupling: (1) between NPs within the self-assembled array and (2) between the TiN/Ag substrate and the NP array.

Characteristic reflectance and SERS spectra arise from the formation of NP arrays at the SLI. First, the plasmonically active NP array on the substrate almost totally quenched the reflectance at ∼580 nm as shown in Figure 1b-iii (red curve). Compared with previous studies using smaller, 16 nm NPs,[43] the reflectance dip here can be red-shifted to 580 nm and deepened to −90%. More importantly, SERS "hot spots" are formed not only among the NP array but also between the substrate and the array, where the Raman signals of 4-MBA are significantly enhanced. As shown in Figure 1c-iii, the red curve, when 0.7 V vs PZC potential is applied, the two characteristic Raman peaks[49] for 4-MBA at 1078 and 1589 cm^{-1} significantly increase in intensity.

The plasmonic coupling between metallic NPs has been studied extensively, but the coupling between a metallic substrate and an electro-variable 2D NP array is still intriguing from both experimental and theoretical viewpoints. In Figure 1b,c, comparisons of optical reflectivity and SERS signals are made between the Au NP array on TiN/glass substrate (panel i) and on TiN/Ag substrate (panels ii and iii). It is easy to see a peak in the reflectance spectra of the NPs/TiN/glass at 0.7 V vs PZC (Figure 1b-i), which is very much like that of an array of NPs at the liquid | liquid interface[42,47] showing the enhancement of reflectance near the wavelength of the plasmon resonance in the array of gold NPs. On theTiN/Ag substrate, the NP array formed under 0.7 V vs PZC, however, quenches the reflectivity of the substrate to such an extent that the reflectance around 580 nm is even lower than for the lone NP array. Both effects are in accordance with our previous studies.[42−44]

This phenomenon of quenching of reflection on the NPs/TiN/Ag sample demonstrates the efficient coupling between the array of electrosorbed large, 40 nm NPs and the metallic substrate, which also gives rise to the enhancement of Raman signal. When the array of 4-MBA functionalized NPs is self-assembled on the TiN/glass substrate under 0.7 V vs PZC, the sample gives a distinguishable Raman signal (∼3000 counts at 1078 cm^{-1}) due to the coupling among the NPs (Figure 1c-i, red curve). By comparison, once those NPs are assembled on the TiN/Ag substrate (under 0.7 V vs PZC), the intensity of the Raman peak increases by ∼8.3 fold (Figure 1c-iii), highlighting the synergistic effect between the NP array and the TiN/Ag substrate. Unlike NP aggregates, the interparticle distance could be uniformly controlled bringing about good uniformity and reproducibility of the Raman signal, as shown in Figure S6. Notably, the pH has a significant influence on the stability of the NPs and the density of the NP array assembled at the SLI. As previously reported,[43,50] a lower pH reduces the negative charge on the carboxylic acid functionalized NPs facilitating the formation of denser NP arrays (Figure S7 and Figure S8). As shown in Figure S8, a higher pH induces weaker plasmonic coupling: shallower reflectance dip, larger interparticle gap, and lower SERS signal. This is consistent with an increased negative charge and hence increased electrostatic repulsion between the NPs. This in turn results in the formation of less densely packed NP arrays at the SLI. Therefore, to maintain the stability of the NP solution while achieving a good SERS signal, a pH of 6.2 was used for normal operational conditions.

The detailed electrotunable behaviors of this system were examined through reflectance and SERS at varying potentials. A qualitative view of the effect on NP assembly as a function of potential is shown in the SEMs in Figure 2a. However, it should be noted that the drying process for SEM sample preparation can potentially disturb the arrangement of the wet NPs on the substrates. Nevertheless, an increase in potential applied before drying results in an increase in NP density. This increased population and its resultant enhanced plasmonic coupling can be visualized by the dramatic changes in the macroscale colors of the wet samples (inset of Figure 2a). Starting from the original silver color of the pristine substrate, higher potential delivers redder and darker appearance and ultimately a purplish black color for the 0.7 V vs PZC sample.

Reflectance measurements and theoretical calculations provide more quantitative insight for this electro-variable phenomenon. With the increase of the applied potential, a distinctive reflectance dip gets deeper and red-shifted, as can be seen from excellently matched experimental and theoretical fitted spectra (Figure 2b,c). Within the lower potential region (<0.4 V vs PZC), both the dip depth (Figure S9) and dip wavelength (Figure 2d) change slowly. Theoretical calculation (Figure 2d) indicates that the interparticle distances in these cases are too large to generate effective plasmonic coupling. Further increase in potential induces dramatic optical changes: the dip wavelength red-shifts from 530 to 580 nm, while the dip depth changes from almost zero to −92%. This can be explained by the strong plasmonic coupling when NPs are getting closer to each other. The reason why they are getting closer was described by us already.[43] At positive electrode potentials, negatively charged NPs get electrosorbed at the electrode, but as they electrostatically repel each other, they prefer not to come close to each other. With further increase of the positive potential, the driving force for each NPs to be adsorbed at the interface gets stronger, and more NPs adsorb at the electrode, tolerating interparticle repulsion, and hence the NP-array gets denser.[51] The results of fitting the theoretical reflectance spectra to the experimental ones (Figure 2d) with the average inter NP distance as the fitting parameter indicates that this distance starts from several hundreds of nm at 0.1 V vs PZC, and quickly reduces to 20 nm at 0.7 V vs PZC.

On the basis of the electromagnetic mechanism of SERS, the variation of the plasmonic coupling due to the change of the interfacial potential also offers a unique and convenient way to enhance the Raman signals. When the potential is low, the two characteristic peaks at 1078 and 1589 cm^{-1} are almost indistinguishable from the base lines (Figure 2e). The intensity of these peaks climbs gradually (in an almost linear fashion) when the potential is less than 0.4 V vs PZC, but more instructive is the linear dependence on the density of the NP array, which is inversely proportional to the square of interparticle separation, shown in the inset in Figure 2f. Such linear dependence shows that the increase in the SERS intensity here is just due to the increase of the population of NPs and the associated 4-MBA at the interface. As the

DOI: 10.1021/acsnano.9b05257
ACS Nano 2020, 14, 328−336

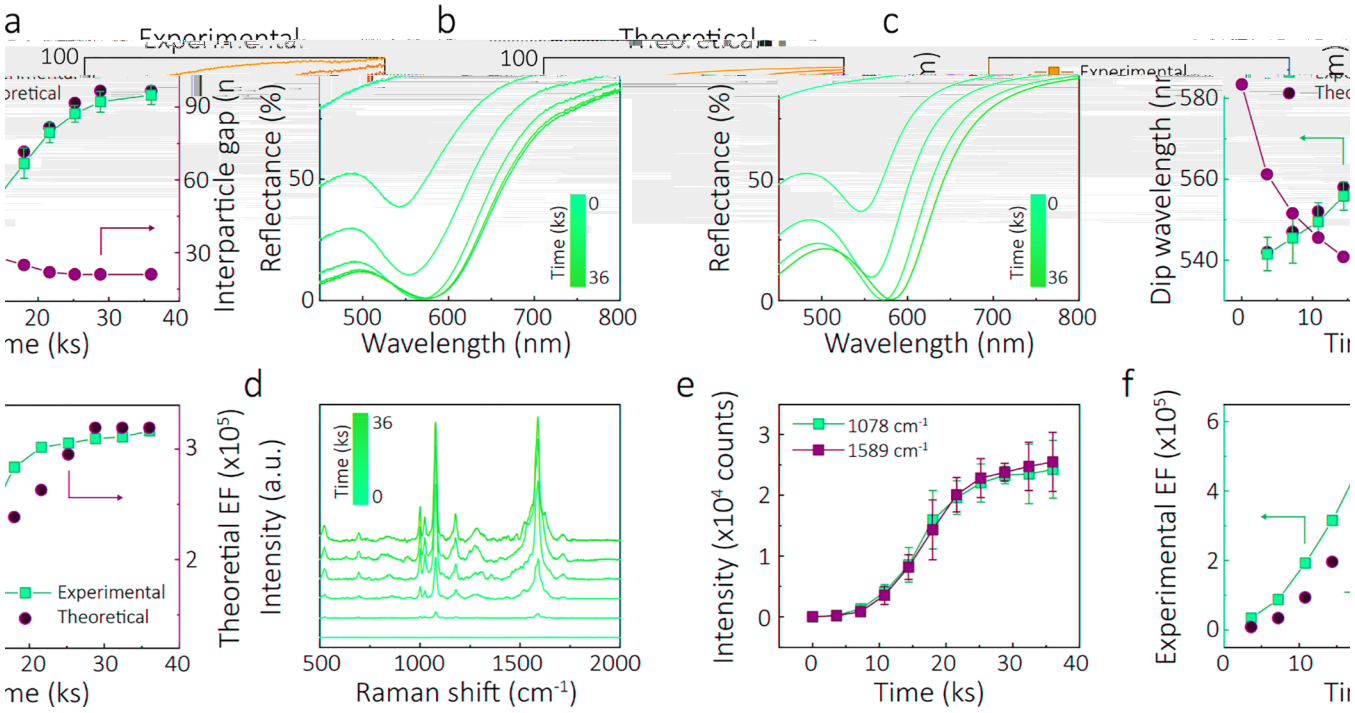

Figure 3. Kinetics of nanoparticle assembly. (a) The time-dependent reflectance spectra of NPs electrosorbed on TiN/Ag in 20 mM PB, 20 mM LiCl NP solution, under 0.7 V vs PZC, starting from pristine TiN/Ag. (b) The theoretically fitted time-dependent reflectance spectra of NPs assembling on TiN/Ag. (c) Time-dependent experimental, theoretically fitted dip wavelength (orange squares), and the theoretically calculated interparticle gap (blue dots). (d) Time-dependent SERS spectra of 4-MBA attached to NPs assembling on TiN/Ag in 20 mM PB, 20 mM LiCl at 0.7 V vs PZC, starting from pristine TiN/Ag. (e) Corresponding experimental time-dependent intensity of characteristic SERS peaks of 4-MBA at 1078 cm^{-1} (orange) and 1589 cm^{-1} (blue). (f) Time-dependent experimental (orange squares) and theoretically calculated (blue dots) SERS enhancement factors (EF) for 1078 cm^{-1} under 0.7 V vs PZC, starting from pristine TiN/Ag.

interparticle gap is large within this potential range (Figure 2d), the coupling between NPs is negligible and so is the increase of the corresponding experimental enhancement factor (Figure 2g), $EF = \frac{I_{SERS}/N_{SERS}}{I_{RS}/N_{RS}}$ (where I_{SERS} and I_{RS} denote the intensity of SERS and Raman signals, N_{SERS} and N_{RS} are the numbers of molecules generating SERS and Raman signals, respectively). In this potential range, each electrosorbed NP individually delivers a hot spot between it and the substrate. However, the hotter ones emerge only at the closer approach of NPs due to the coupling of the localized plasmon excitations between the NPs, presumably amplified by the proximity to the metallic substrate.

As the potential increases beyond 0.4 V vs PZC, the intensities of the peaks rocket to ~25 000 counts at 0.7 V vs PZC; both the experimental and theoretical (cf. Methods) EFs surge quickly to reach beyond 10^5 level at 0.7 V vs PZC. This means that the amplification of the SERS signal benefits majorly not only from the increased number of NPs and 4-MBA molecules but also from the ever-growing plasmonic coupling with gradual red-shift of LSPR toward the excitation laser wavelength.[52]

We notice that the experimental EFs are slightly larger than the theoretical ones, were perfectly spherical NPs in a uniform hexagonal lattice was considered for modeling. Considering the existence of edges/spikes on our fabricated NPs and the fact that interparticle gaps may have some dispersion and spatial nonuniformity, a small population of NPs with narrow local interparticle gaps could generate much stronger SERS signals that would contribute to larger experimental values of EF.[26,36]

The time evolution of the optical response and SERS signals were also monitored during the potential controlled assembly of NPs on the substrates. Figure 3a,b demonstrates the experimental and theoretically fitted reflectance spectra over 10 h when both the dip wavelength (Figure 3c) and dip depth (Figure S10) first experience a fast evolution stage before reaching the equilibrium plateau at the 580 nm wavelength and −92% intensity. A similar trend in can be found in the fitted values of the interparticle gaps. Compared with similar systems with smaller NPs, the time of reaching the equilibrium for our 40 nm NPs is longer because of their larger diameter and correspondingly smaller diffusion coefficient (usually following the Stokes−Einstein equation).[53] Nevertheless, higher NP concentrations and shorter diffusion lengths in miniaturized setups could accelerate this process for practical applications.

It should be emphasized again, as we have seen first in Figure 1b, that Figures 2b and 3a demonstrate the counter-intuitive effect of quenching of reflection from an array of large NPs on metallic substrates at the wavelength of the coupled plasmon resonance, the signatures of which have been predicted earlier theoretically.[44,54,55] The change in SERS signal follows a slightly different pattern upon application of a positive bias (Figure 3d). Unlike the fast quenching process of the reflectivity in the initial stage, the intensities of the Raman peaks grow relatively slowly (Figure 3e). Generally speaking, the plasmonic coupling and the resultant Raman enhancement prevail only when the gaps between NPs are below the NP diameter.[56] Considering the interparticle gaps in the first 14 ks is still larger than this value (Figure 3c), the Raman hot spots are still too weak to generate a noticeable enhanced

DOI: 10.1021/acsnano.9b05257
ACS Nano 2020, 14, 328−336

Raman signal when compared to individual NPs. However, this hot spot effect becomes more dominant after 14 ks when the gap falls below 40 nm. The calculated experimental and theoretical EFs in Figure 3f support this observation.

The electrotunability and reversibility of SERS signal is always desirable for reusable sensors, for lasers with different working frequencies or sensing different analytes. Though larger NPs provide stronger SERS amplifications, it is harder to achieve reversibility with larger NPs as compared with smaller ones because of the reduced diffusion speed of the former.[57] Here by alternatively applying ±0.7 V vs PZC to the substrate, we partially achieved turning the system on and off for multiple times. As shown in Figure 4a, under the "off state" at −0.7 V vs PZC, the plain substrate has a pink tint, and the red letter "IC" (standing for Imperial College) above the substrate is reflected distinctively. In contrast to that, the substrate becomes almost black, and the "IC" is overwhelmed by the dark background under the "on state" at 0.7 V vs PZC.

The cycling of the reflectance spectra as shown in Figure 4b and Figure S11 demonstrate that the "on state" is always reversible. However, in the electrode potential range that we have studied under the "off state", there are always a few NPs stuck at the interface. This results in a small reflection dip and small Raman peaks. Fitting the theory of the optical spectra to the measured reflectance data provides evidence (Figure 4d) that the "off state" corresponds to an 80 nm interparticle gap. To summarize, at −0.7 V the majority of NPs desorb from the solid interface to the bulk; however, some remain behind. Had we been able to apply more negative potentials, we would have expected to have no NPs left at the interface. It cannot be excluded, however, that for more negative potentials, there could be some metastable well, which could kinetically trap NPs at the interface (cf. kinetics of collective desorption of NPs).[43]

Importantly, much like conventional SERS substrates, the platform could be used to simultaneously detect and distinguish multiple analytes. This was shown for NPs functionalized with 2-mercapto-5-nitrobenzimidazole (MNBI), malachite green isothiocyanate (MG) and MBA (Figure S12). In addition, we also examined the influence of serum to the Raman signal of the assembled MBA functionalized NPs. As shown in Figure S13, no additional peaks could be observed after the addition of serum, though the intensity of MBA peaks are slightly reduced likely due to scattering of the suspension. Nevertheless, this platform opens the door to the possibility of using such systems for biosensing applications.

CONCLUSIONS

We investigated the optical response of an electrotunably assembling two-dimensional array of Au NPs on a TiN/Ag electrode under different electrode potentials. Increasing positive polarization of the electrode stimulates adsorption of negatively charged nanoparticles, decreasing interparticle separations in the array. The narrowing of the interparticle gaps strengthens the plasmonic coupling between NPs. As a consequence, it produces three related effects: (1) The emergence of the dip in the reflection spectrum, which gets deeper and its wavelength shifts to the longer wavelength with densification of the NP array. (2) The emergence and further intensification of "hot spots" between NPs, in addition to the hot spots between individual NPs and the substrate. (3) The red-shifting of the coupled plasmon resonance of the thus-assembled NPs toward the wavelength of Raman excitation

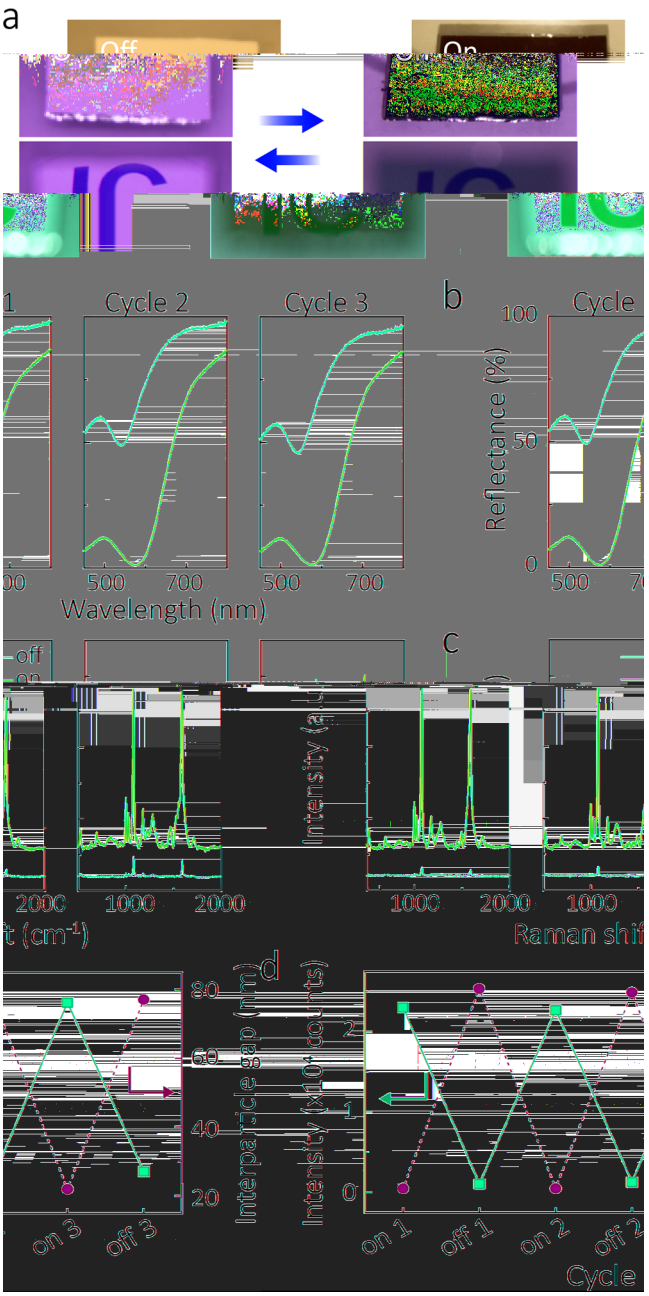

Figure 4. Reversible switching of nanoparticles at a solid | liquid interface. To switch off the system, a low potential (−0.7 V vs PZC) is applied to the substrate and maintained for 5 min. (a) The digital camera photos of the "off" and "on" states of the system in solution with plain (upper), and "IC" reflected (lower) images. The letters are drawn on A4 paper in red and are illuminated by white light. (b) Reflectance spectra of the NP array on TiN/Ag during multiple on/off cycles. (c) Raman spectra of 4-MBA modified NP array on TiN/Ag during multiple on/off cycles. (d) The Raman intensity (orange) and the calculated interparticle gaps (blue) for multiple on/off cycles are plotted.

laser further amplifies SERS signal from analytes attached to NPs.

The theory of reflection signal from such systems allows us to quantify the values of interparticle gaps at any applied potential and use this information to estimate the SERS enhancement factor. The SERS data appear to be in full harmony with the reflectivity data. The experimental results

DOI: 10.1021/acsnano.9b05257
ACS Nano 2020, 14, 328−336

Table 1. Parameters of the Drude−Lorentz model for Au, TiN, and Ag

material	ε_∞	$\omega_{p,D}$ (eV)	γ_D (eV)	s_1	$\omega_{p1,L}$ (eV)	$\gamma_{1,L}$ (eV)	s_2	$\omega_{p2,L}$ (eV)	$\gamma_{2,L}$ (eV)
Au	5.9752	8.8667	0.03799	1.76	3.6	1.3	0.952	2.8	0.737
TiN[a]	2.667	10.707	0.195	0.195	2.264	0.722	5.312	4.894	3.875
Ag	3.718	9.2093	0.02	0.4242	4.284	0.737	-	-	-

[a]The parameters for TiN coating are slightly different to that of the bulk TiN, as these are fitted to match the measured optical reflectance from a bare 5 nm TiN coating on top of an Ag substrate.

show the earlier theoretically predicted counterintuitive phenomenon—*complete quenching of reflection* from an array of large NPs on metallic substrates at the wavelength of the coupled plasmon resonance.

An outlook of this system is to miniaturize it into microscale chips. This will not only make the switching speed faster but also provide an opportunity to be coupled with microfluids feeding different kinds of NPs targeting/reporting different analytes, which offers a promising approach of high-throughput optical sensing with electro-tunability and reusability.

METHODS

Materials and Experimental Setup. *4-MBA Capped 40 nm Gold Nanoparticles.* First, 16 nm NPs were synthesized according to the Frens[58] method: A solution of 500 mL 0.01 wt % $HAuCl_4$ was heated to boil with magnetic stirring, followed by the injection of 10 mL of 1 wt % sodium citrate, which was kept for 30 min to allow the reaction to finish. The resultant red NP solution was then cooled to room temperature. Then 40 nm NPs was synthesized according to the Brown method.[59] Namely, 540 mL of water was mixed into 60 mL of previously obtained 16 nm NP solution. Followed by the addition of 6 mL of 0.2 M $NH_2OH{\cdot}HCl$, 5 mL of 1 wt % $HAuCl_4$ was quickly injected with vigorous stirring. After the reaction finished, 612 μL of 10 mM solution of 80% 4-mercaptobenzoic acid (MBA) and 20% 12-mercaptododecanoic acid (MDDA) was added into the solution, which was allowed 12 h for functionalization. Centrifugation of the NPs were performed at 3000 rpm for 1 h and refilled with DI water. We checked the diameter of NPs (Figures S2a) by transmission electron microscope (TEM, JEOL 2100 PLUS), the absorption spectra (Figure S2c) of NPs by a UV−vis spectrometer (Nanodrop 2000, Thermo Scientific), and the presence of NPs on substrates by scanning electron microscope (SEM, LEO Gemini 1525 FEGSEM).

Functionalization with 2-Mercapto-5-nitrobenzimidazole (MNBI) and Malachite Green Isothiocyanate (MG). MNBI- and MG-functionalized NPs were prepared as follows: 612 μL of 10 mM solution of 80% MBNI and 20% MDDA or 612 μL of 1 mM MG and 10 mM MDDA solution was added into the 40 nm citrate-functionalized NP solution, respectively, and allowed 12 h for functionalization. The dual functionalized MBA-MBNI or MBA-MG NPs were prepared by adding 100 nM MBNI or MG into the above-mentioned MBA NP solutions, respectively, and allowed to rest for 12 h prior to centrifugation.

TiN/Ag Substrates. Similar to previous plasma-enhanced atomic layer deposition (PEALD) method,[43] silicon substrates were first stripped of their native oxide layer in a hydrofluoric acid bath. A 2 nm Ti adhesion layer was then evaporated onto the substrate, followed by a 125 nm Ag layer. The sample was then immediately placed in a PEALD system (Veeco Fiji system), where 5 nm of TiN was deposited at a temperature of 270 °C. The sample was left to cool in the chamber before exposing it to atmosphere in order to avoid excessive oxidation. Before use, the TiN/Ag substrates were intensively rinsed by acetone, ethanol, and DI water.

Coupled Electrochemical-Optical Setup and Measurements. A TiN/Ag substrate acting as the working electrode was inserted into a polytetrafluoroethylene (PTFE) holder which connects the substrate with a platinum wire leading to the potentiostat. Two other holes on the holder accommodated the Ag/AgCl reference electrode and platinum counter electrode, to constitute a three-electrode system. A Gamry ref-600 potentiostat was used to control cell polarization. A purpose-built Raman microscope is based on an optical inverted microscope (IX71, Olympus), to which a spectrograph (Shamrock SR-303i, Andor) and an electron-multiplying charge-coupled device camera (EMCCD, Newton DU970BV, Andor) were connected. An Olympus 20×, NA 0.45 objective (LCPLFLN-LCD) was mounted on the microscope to focus 0.81 mW power from a 632.8 nm laser beam emitted from a HeNe laser (HRP170, Thorlabs, 21 mW). The reflectance spectra were measured using an Ocean Optics reflection probe with a focal length of 2 mm, which was placed above the substrate normal to the TiN/Ag substrate. The white light emitted by a tungsten halogen lamp (Ocean Optics) was transmitted through a multimode fiber in the probe, hit the substrate, and was collected by an Andor 163 spectrograph fitted with an iDus charge-coupled device. All the optical references are derived from a Thorlabs silver mirror. During the measurements, NP solution with 20 mM phosphate buffer (pH 6.2) and 20 mM LiCl electrolyte was poured into the cell. The use of phosphate buffer was used to keep the pH stable during the experiments, and the LiCl was used to adjust the electrolyte concentration and to provide Cl^- ions for Ag/AgCl reference electrode. NPs were found to be more stable in LiCl than in standard NaCl solution (Figure S3). The Gamry potentiostat applied potential to the substrate while the synchronized Andor spectrometer collected the reflected signals from the substrate simultaneously.

Theoretical Methods. *Theoretical Calculation of Optical Reflectance Spectra.* A five-layer stack model, based on our effective medium theory and multilayer Fresnel reflection scheme, was deployed to theoretically calculate the optical reflectance spectra. The detail of the theoretical model is provided.[44] The following parameters, conditions, and entities were used for the calculations based on that theoretical model: NP radius R = 20 nm; normal incidence angle (as the data were obtained at such angle); ε_1 = 1.78, representing an aqueous solution as the NP surrounding medium; $\varepsilon_2(\omega)$, denoting a fictitious film emulating the Au NP monolayer, calculated using eq (5) in ref 44; ε_3 = 1.78 for the spacer layer of thickness h_s = 1 nm between the NPs and the TiN/Ag substrate; $\varepsilon_4(\omega) = \varepsilon_{TiN}$ representing a thin TiN coating, of thickness h_f = 5 nm, on top of a 125 nm-thick Ag film substrate characterized by $\varepsilon_5(\omega) = \varepsilon_{Ag}$. Note that the Ag substrate is thick enough not to allow any transmittance through it, and hence, it was safe to be modeled as a semi-infinite layer. The parameters of the Drude−Lorentz model[44] used to describe optical response of Au (eventually used to obtain $\varepsilon_2(\omega)$), TiN, and Ag are provided in Table 1.

Calculation of Theoretical SERS EFs. Numerical simulation of the near-field distribution patterns of the Au NP assembly on TiN/Ag substrate provided theoretical estimates of the SERS EFs, calculated as $\max(|\boldsymbol{E}/\boldsymbol{E}_0|^4)$, where $\boldsymbol{E}/\boldsymbol{E}_0$ is the local electric field enhancement factor at the wavelength of the reflectance dip. The full-wave simulations were conducted using the RF module of the COMSOL Multiphysics, a commercially available finite-element-method software. In the simulation model, perfectly spherical Au nanospheres were arranged in a hexagonal lattice on top of a TiN/Ag-substrate film of the thicknesses specified in the experiments. A unit cell was designed, which extended in both lateral dimensions using periodic boundary conditions to emulate a NP monolayer assembled on the TiN/Ag substrate with large lateral dimensions. Frequency domain solver was deployed for the simulation studies with extremely small meshing, where the maximum and the minimum mesh element size was chosen to be $\lambda/10$ (where λ is the wavelength of light in that medium) and 1.5 nm, respectively. Such dense meshing incorporates

DOI: 10.1021/acsnano.9b05257
ACS Nano 2020, 14, 328−336

fine structural details of the system in the numerical simulations and hence allows to make a good estimation of the SERS EFs.

ASSOCIATED CONTENT

Supporting Information

The Supporting Information is available free of charge at https://pubs.acs.org/doi/10.1021/acsnano.9b05257.

Setup of the electrochemical cell, TEM and UV−vis data about gold NPs, the influence of electrolyte, potential of zero charge, cyclic voltammogram, SERS intensity mapping, the influence of pH, static and dynamic dip depth of the reflectance, reversibility, the calculation of EF, detecting multiple analytes through SERS and the Raman spectra of NP array in serum (PDF)

AUTHOR INFORMATION

Corresponding Authors

*E-mail: a.kornyshev@imperial.ac.uk.
*E-mail: joshua.edel@imperial.ac.uk.

ORCID

Sang-Hyun Oh: 0000-0002-6992-5007
Anthony R. J. Kucernak: 0000-0002-5790-9683
Alexei A. Kornyshev: 0000-0002-3157-8791
Joshua B. Edel: 0000-0001-5870-8659

Notes

The authors declare no competing financial interest.

ACKNOWLEDGMENTS

The work was supported by an Engineering and Physical Sciences Research Council grant, "Electrotunable Molecular Alarm", EP/L02098X/1. J.B.E. also acknowledges receipt of European Research Council consolidator grant (NanoPD). Y.M. has been supported in part by a China Scholarship Council-Imperial Scholarship (201506320194). L.V. and D.S. acknowledge the support of Marie Skłodowska-Curie fellowships, N-SHEAD and S-OMMs, respectively. D.J.K. and S.-H.O. acknowledge support from Seagate Technology through the Centre for Micromagnetics and Information Technologies (MINT) at the University of Minnesota.

REFERENCES

(1) Sikdar, D.; Kornyshev, A. A. Theory of Tailorable Optical Response of Two-Dimensional Arrays of Plasmonic Nanoparticles at Dielectric Interfaces. *Sci. Rep.* **2016**, *6*, 33712.

(2) Solís, D. M.; Taboada, J. M.; Obelleiro, F.; Liz-Marzán, L. M.; García de Abajo, F. J. Optimization of Nanoparticle-Based SERS Substrates through Large-Scale Realistic Simulations. *ACS Photonics* **2017**, *4*, 329−337.

(3) Nayak, D. R.; Bhat, N.; Venkatapathi, M.; Umapathy, S. Signal Enhancement from Tunable SERS Substrates: Design and Demonstration of Multiple Regimes of Enhancement. *J. Phys. Chem. C* **2018**, *122*, 9134−9140.

(4) Stewart, M. E.; Anderton, C. R.; Thompson, L. B.; Maria, J.; Gray, S. K.; Rogers, J. A.; Nuzzo, R. G. Nanostructured Plasmonic Sensors. *Chem. Rev.* **2008**, *108*, 494−521.

(5) Domenici, F.; Fasolato, C.; Mazzi, E.; De Angelis, L.; Brasili, F.; Mura, F.; Postorino, P.; Bordi, F. Engineering Microscale Two-Dimensional Gold Nanoparticle Sluster Arrays for Advanced Raman Sensing: an AFM Study. *Colloids Surf., A* **2016**, *498*, 168−175.

(6) Fasolato, C.; Giantulli, S.; Silvestri, I.; Mazzarda, F.; Toumia, Y.; Ripanti, F.; Mura, F.; Luongo, F.; Costantini, F.; Bordi, F.; Postorino, P.; Domenici, F. Folate-Based Single Cell Screening Using Surface Enhanced Raman Microimaging. *Nanoscale* **2016**, *8*, 17304−17313.

(7) Giannini, V.; Fernandez-Dominguez, A. I.; Heck, S. C.; Maier, S. A. Plasmonic Nanoantennas: Fundamentals and Their Use in Controlling the Radiative Properties of Nanoemitters. *Chem. Rev.* **2011**, *111*, 3888−3912.

(8) Jain, P. K.; Huang, X. H.; El-Sayed, I. H.; El-Sayed, M. A. Noble Metals on the Nanoscale: Optical and Photothermal Properties and Some Applications in Imaging, Sensing, Biology, and Medicine. *Acc. Chem. Res.* **2008**, *41*, 1578−1586.

(9) Fasolato, C.; Giantulli, S.; Capocefalo, A.; Toumia, Y.; Notariello, D.; Mazzarda, F.; Silvestri, I.; Postorino, P.; Domenici, F. Antifolate SERS-Active Nanovectors: Quantitative Drug Nanostructuring and Selective Cell Targeting for Effective Theranostics. *Nanoscale* **2019**, *11*, 15224−15233.

(10) Liu, B.; Yao, X.; Chen, S.; Lin, H.; Yang, Z.; Liu, S.; Ren, B. Large-Area Hybrid Plasmonic Optical Cavity (HPOC) Substrates for Surface-Enhanced Raman Spectroscopy. *Adv. Funct. Mater.* **2018**, *28*, 1802263.

(11) Wang, X. T.; Ma, G. S.; Li, A. R.; Yu, J.; Yang, Z.; Lin, J.; Li, A.; Han, X. D.; Guo, L. Composition-Adjustable Ag-Au Substitutional Alloy Microcages Enabling Tunable Plasmon Resonance for Ultrasensitive SERS. *Chem. Sci.* **2018**, *9*, 4009−4015.

(12) Xu, Y.; Konrad, M. P.; Lee, W. W. Y.; Ye, Z.; Bell, S. E. J. A Method for Promoting Assembly of Metallic and Nonmetallic Nanoparticles into Interfacial Monolayer Films. *Nano Lett.* **2016**, *16*, 5255−5260.

(13) Su, D.; Jiang, S. L.; Yu, M. N.; Zhang, G. Z.; Liu, H.; Li, M. Y. Facile Fabrication of Configuration Controllable Self-Assembled Al Nanostructures as UV SERS Substrates. *Nanoscale* **2018**, *10*, 22737−22744.

(14) Tian, L.; Su, M.; Yu, F.; Xu, Y.; Li, X.; Li, L.; Liu, H.; Tan, W. Liquid-State Quantitative SERS Analyzer on Self-Ordered Metal Liquid-Like Plasmonic Arrays. *Nat. Commun.* **2018**, *9*, 3642.

(15) Fasolato, C.; Domenici, F.; Sennato, S.; Mura, F.; De Angelis, L.; Luongo, F.; Costantini, F.; Bordi, F.; Postorino, P. Dimensional Scale Effects on Surface Enhanced Raman Scattering Efficiency of Self-Assembled Silver Nanoparticle Clusters. *Appl. Phys. Lett.* **2014**, *105*, 073105.

(16) Domenici, F.; Bizzarri, A. R.; Cannistraro, S. Surface-Enhanced Raman Scattering Detection of Wild-Type and Mutant p53 Proteins at Very Low Concentration in Human Serum. *Anal. Biochem.* **2012**, *421*, 9−15.

(17) Su, M.; Li, X.; Zhang, S.; Yu, F.; Tian, L.; Jiang, Y.; Liu, H. Self-Healing Plasmonic Metal Liquid as a Quantitative Surface-Enhanced Raman Scattering Analyzer in Two-Liquid-Phase Systems. *Anal. Chem.* **2019**, *91*, 2288−2295.

(18) Lalander, C. H.; Zheng, Y.; Dhuey, S.; Cabrini, S.; Bach, U. DNA-Directed Self-Assembly of Gold Nanoparticles onto Nanopatterned Surfaces: Controlled Placement of Individual Nanoparticles into Regular Arrays. *ACS Nano* **2010**, *4*, 6153−6161.

(19) Srituravanich, W.; Fang, N.; Sun, C.; Luo, Q.; Zhang, X. Plasmonic Nanolithography. *Nano Lett.* **2004**, *4*, 1085−1088.

(20) Chen, S.-Y.; Mock, J. J.; Hill, R. T.; Chilkoti, A.; Smith, D. R.; Lazarides, A. A. Gold Nanoparticles on Polarizable Surfaces as Raman Scattering Antennas. *ACS Nano* **2010**, *4*, 6535−6546.

(21) Wang, X.; Li, M.; Meng, L.; Lin, K.; Feng, J.; Huang, T.; Yang, Z.; Ren, B. Probing the Location of Hot Spots by Surface-Enhanced Raman Spectroscopy: Toward Uniform Substrates. *ACS Nano* **2014**, *8*, 528−536.

(22) Ding, L.; Gao, Y.; Di, J. A Sensitive Plasmonic Copper(II) Sensor Based on Gold Nanoparticles Deposited on ITO Glass Substrate. *Biosens. Bioelectron.* **2016**, *83*, 9−14.

(23) Yan, B.; Thubagere, A.; Premasiri, W. R.; Ziegler, L. D.; Dal Negro, L.; Reinhard, B. M. Engineered SERS Substrates with Multiscale Signal Enhancement: Nanoparticle Cluster Arrays. *ACS Nano* **2009**, *3*, 1190−1202.

(24) Kim, I. H.; Kim, J. H.; Choi, J. Y.; Shin, C. H.; Kim, J. H.; Bae, G. T.; Shin, K. S. Tuning the Interparticle Distances in Self-Assembled Gold Nanoparticle Films with Their Plasmonic Responses. *Chem. Phys. Lett.* **2019**, *715*, 91−99.

DOI: 10.1021/acsnano.9b05257
ACS Nano 2020, 14, 328−336

(25) Ashley, M. J.; Bourgeois, M. R.; Murthy, R. R.; Laramy, C. R.; Ross, M. B.; Naik, R. R.; Schatz, G. C.; Mirkin, C. A. Shape and Size Control of Substrate-Grown Gold Nanoparticles for Surface-Enhanced Raman Spectroscopy Detection of Chemical Analytes. *J. Phys. Chem. C* **2018**, *122*, 2307−2314.
(26) Huang, Z. L.; Meng, G. W.; Hu, X. Y.; Pan, Q. J.; Huo, D. X.; Zhou, H. J.; Ke, Y.; Wu, N. Q. Plasmon-tunable Au@Ag Core-Shell Spiky Nanoparticles for Surface-Enhanced Raman Scattering. *Nano Res.* **2019**, *12*, 449−455.
(27) Du, Y. X.; Wei, W.; Zhang, X. W.; Li, Y. B. Tuning Metamaterials Nanostructure of Janus Gold Nanoparticle Film for Surface-Enhanced Raman Scattering. *J. Phys. Chem. C* **2018**, *122*, 7997−8002.
(28) Kanipe, K. N.; Chidester, P. P. F.; Stucky, G. D.; Moskovits, M. Large Format Surface-Enhanced Raman Spectroscopy Substrate Optimized for Enhancement and Uniformity. *ACS Nano* **2016**, *10*, 7566−7571.
(29) Hill, R. T.; Mock, J. J.; Urzhumov, Y.; Sebba, D. S.; Oldenburg, S. J.; Chen, S.-Y.; Lazarides, A. A.; Chilkoti, A.; Smith, D. R. Leveraging Nanoscale Plasmonic Modes to Achieve Reproducible Enhancement of Light. *Nano Lett.* **2010**, *10*, 4150−4154.
(30) Edel, J. B.; Kornyshev, A. A.; Kucernak, A. R.; Urbakh, M. Fundamentals and Applications of Self-Assembled Plasmonic Nanoparticles at Interfaces. *Chem. Soc. Rev.* **2016**, *45*, 1581−1596.
(31) Laible, F.; Gollmer, D. A.; Dickreuter, S.; Kern, D. P.; Fleischer, M. Continuous Reversible Tuning of the Gap Size and Plasmonic Coupling of Bow Tie Nanoantennas on Flexible Substrates. *Nanoscale* **2018**, *10*, 14915−14922.
(32) Lu, X. F.; Huang, Y. J.; Liu, B. Q.; Zhang, L.; Song, L. P.; Zhang, J. W.; Zhang, A. F.; Chen, T. Light-Controlled Shrinkage of Large-Area Gold Nanoparticle Monolayer Film for Tunable SERS Activity. *Chem. Mater.* **2018**, *30*, 1989−1997.
(33) Han, F.; Vivekchand, S. R. C.; Soeriyadi, A. H.; Zheng, Y.; Gooding, J. J. Thermoresponsive Plasmonic Core−Satellite Nanostructures with Reversible, Temperature Sensitive Optical Properties. *Nanoscale* **2018**, *10*, 4284−4290.
(34) Ma, Y.; Sikdar, D.; Fedosyuk, A.; Velleman, L.; Zhao, M.; Tang, L.; Kornyshev, A. A.; Edel, J. B. An Auxetic Thermo-Responsive Nanoplasmonic Optical Switch. *ACS Appl. Mater. Interfaces* **2019**, *11*, 22754−22760.
(35) Curtis, T.; Taylor, A. K.; Alden, S. E.; Swanson, C.; Lo, J.; Knight, L.; Silva, A.; Gates, B. D.; Emory, S. R.; Rider, D. A. Synthesis and Characterization of Tunable, pH-Responsive Nanoparticle−Microgel Composites for Surface-Enhanced Raman Scattering Detection. *ACS Omega* **2018**, *3*, 10572−10588.
(36) Velleman, L.; Scarabelli, L.; Sikdar, D.; Kornyshev, A. A.; Liz-Marzan, L. M.; Edel, J. B. Monitoring Plasmon Coupling and SERS Enhancement through *In Situ* Nanoparticle Spacing Modulation. *Faraday Discuss.* **2017**, *205*, 67−83.
(37) Edel, J. B.; Kornyshev, A. A.; Urbakh, M. Self-Assembly of Nanoparticle Arrays for Use as Mirrors, Sensors, and Antennas. *ACS Nano* **2013**, *7*, 9526−9532.
(38) Lumdee, C.; Toroghi, S.; Kik, P. G. Post-Fabrication Voltage Controlled Resonance Tuning of Nanoscale Plasmonic Antennas. *ACS Nano* **2012**, *6*, 6301−6307.
(39) Di Martino, G.; Turek, V. A.; Lombardi, A.; Szabó, I.; de Nijs, B.; Kuhn, A.; Rosta, E.; Baumberg, J. J. Tracking Nanoelectrochemistry Using Individual Plasmonic Nanocavities. *Nano Lett.* **2017**, *17*, 4840−4845.
(40) Byers, C. P.; Hoener, B. S.; Chang, W.-S.; Link, S.; Landes, C. F. Single-Particle Plasmon Voltammetry (spPV) for Detecting Anion Adsorption. *Nano Lett.* **2016**, *16*, 2314−2321.
(41) Zdaniauskienė, A.; Charkova, T.; Matulaitienė, I.; Eicher-Lorka, O.; Matijoška, A.; Skapas, M.; Selskis, A.; Niaura, G. Electrochemical Shell-Isolated Nanoparticle-Enhanced Raman Spectroscopy: Bonding, Structure, and Ion-Pairing of the Positive Charge Bearing Pyridinium Ring Terminated Monolayer at Smooth Gold Electrode. *J. Phys. Chem. C* **2018**, *122*, 1234−1242.
(42) Montelongo, Y.; Sikdar, D.; Ma, Y.; McIntosh, A. J. S.; Velleman, L.; Kucernak, A. R.; Edel, J. B.; Kornyshev, A. A. Electrotunable Nanoplasmonic Liquid Mirror. *Nat. Mater.* **2017**, *16*, 1127−1135.
(43) Ma, Y.; Zagar, C.; Klemme, D. J.; Sikdar, D.; Velleman, L.; Montelongo, Y.; Oh, S.-H.; Kucernak, A. R.; Edel, J. B.; Kornyshev, A. A. A Tunable Nanoplasmonic Mirror at an Electrochemical Interface. *ACS Photonics* **2018**, *5*, 4604−4616.
(44) Sikdar, D.; Hasan, S. B.; Urbakh, M.; Edel, J. B.; Kornyshev, A. A. Unravelling the Optical Responses of Nanoplasmonic Mirror-on-Mirror Metamaterials. *Phys. Chem. Chem. Phys.* **2016**, *18*, 20486−20498.
(45) Cecchini, M. P.; Wiener, A.; Turek, V. A.; Chon, H.; Lee, S.; Ivanov, A. P.; McComb, D. W.; Choo, J.; Albrecht, T.; Maier, S. A.; Edel, J. B. Rapid Ultrasensitive Single Particle Surface-Enhanced Raman Spectroscopy Using Metallic Nanopores. *Nano Lett.* **2013**, *13*, 4602−4609.
(46) Crick, C. R.; Albella, P.; Kim, H.-J.; Ivanov, A. P.; Kim, K.-B.; Maier, S. A.; Edel, J. B. Low-Noise Plasmonic Nanopore Biosensors for Single Molecule Detection at Elevated Temperatures. *ACS Photonics* **2017**, *4*, 2835−2842.
(47) Velleman, L.; Sikdar, D.; Turek, V. A.; Kucernak, A. R.; Roser, S. J.; Kornyshev, A. A.; Edel, J. B. Tuneable 2D Self-Assembly of Plasmonic Nanoparticles at Liquid|Liquid Interfaces. *Nanoscale* **2016**, *8*, 19229−19241.
(48) McCafferty, E. Relationship between the Isoelectric Point (pHpzc) and the Potential of Zero Charge (Epzc) for Passive Metals. *Electrochim. Acta* **2010**, *55*, 1630−1637.
(49) Orendorff, C. J.; Gole, A.; Sau, T. K.; Murphy, C. J. Surface-Enhanced Raman Spectroscopy of Self-Assembled Monolayers: Sandwich Architecture and Nanoparticle Shape Dependence. *Anal. Chem.* **2005**, *77*, 3261−3266.
(50) Capocefalo, A.; Mammucari, D.; Brasili, F.; Fasolato, C.; Bordi, F.; Postorino, P.; Domenici, F. Exploring the Potentiality of a SERS-Active pH Nano-Biosensor. *Front. Chem.* **2019**, *7*, 413−413.
(51) Zagar, Z.; Rhys-Griffiths, R.; Podgornik, R.; Kornyshev, A. A. On the Voltage-Controlled Assembly of NP Arrays at Electrochemical Solid/Liquid Interfaces. **2018**, *arXiv:1810.05019*, arXiv.org e-Print archive. https://arxiv.org/abs/1810.05019.
(52) Willets, K. A.; Van Duyne, R. P. Localized Surface Plasmon Resonance Spectroscopy and Sensing. *Annu. Rev. Phys. Chem.* **2007**, *58*, 267−297.
(53) Kalathi, J. T.; Yamamoto, U.; Schweizer, K. S.; Grest, G. S.; Kumar, S. K. Nanoparticle Diffusion in Polymer Nanocomposites. *Phys. Rev. Lett.* **2014**, *112*, 108301.
(54) Kornyshev, A. A.; Marinescu, M.; Paget, J.; Urbakh, M. Reflection of Light by Metal Nanoparticles at Electrodes. *Phys. Chem. Chem. Phys.* **2012**, *14*, 1850−1859.
(55) Truong, V. V.; de Dormale, B. Optical Absorption in Overcoats of Nanoparticle Arrays on a Metallic Substrate. *Plasmonics* **2011**, *6*, 195−200.
(56) Le Ru, E. C.; Etchegoin, P. G. Single-Molecule Surface-Enhanced Raman Spectroscopy. *Annu. Rev. Phys. Chem.* **2012**, *63*, 65−87.
(57) Booth, S. G.; Dryfe, R. A. W. Assembly of Nanoscale Objects at the Liquid/Liquid Interface. *J. Phys. Chem. C* **2015**, *119*, 23295−23309.
(58) Frens, G. Controlled Nucleation for the Regulation of the Particle Size in Monodisperse Gold Suspensions. *Nature, Phys. Sci.* **1973**, *241*, 20−22.
(59) Brown, K. R.; Walter, D. G.; Natan, M. J. Seeding of Colloidal Au Nanoparticle Solutions. 2. Improved Control of Particle Size and Shape. *Chem. Mater.* **2000**, *12*, 306−313.

DOI: 10.1021/acsnano.9b05257
ACS Nano 2020, 14, 328−336